



Article

Retrieval of Stratospheric HNO₃ and HCl Based on Ground-Based High-Resolution Fourier Transform Spectroscopy

Changgong Shan ¹, Huifang Zhang ¹, Wei Wang ^{1,*}, Cheng Liu ^{1,2,3}, Yu Xie ⁴ , Qihou Hu ¹ and Nicholas Jones ⁵

¹ Key Laboratory of Environmental Optics and Technology, Anhui Institute of Optics and Fine Mechanics, Chinese Academy of Sciences, Hefei 230031, China; cgshan@aiofm.ac.cn (C.S.); hfzhang@aiofm.ac.cn (H.Z.); chliu81@ustc.edu.cn (C.L.); qhhu@aiofm.ac.cn (Q.H.)

² Department of Precision Machinery and Precision Instrumentation, University of Science and Technology of China, Hefei 230026, China

³ Center for Excellence in Urban Atmospheric Environment, Institute of Urban Environment, Chinese Academy of Sciences, Xiamen 361021, China

⁴ Department of Automation, Hefei University, Hefei 230601, China; xiey@hfu.edu.cn

⁵ School of Earth, Atmospheric and Life Sciences, University of Wollongong, Northfields Ave, Wollongong, NSW 2522, Australia; njones@uow.edu.au

* Correspondence: wwang@aiofm.ac.cn; Tel.: +86-182-5511-2819

Abstract: Vertical profiles and stratospheric HNO₃ and HCl columns are retrieved by ground-based high resolution Fourier transform infrared spectroscopy (FTIR) remote sensing measurements at the Hefei site in China. The time series of stratospheric HNO₃ and HCl columns from January 2017 to December 2019 showed similar annual variation trends, with an annually decreasing rate of $(-9.45 \pm 1.20)\% \text{ yr}^{-1}$ and $(-7.04 \pm 0.81)\% \text{ yr}^{-1}$ for stratospheric HNO₃ and HCl, respectively. The seasonal amplitudes of stratospheric HNO₃ and HCl are $2.67 \times 10^{15} \text{ molec cm}^{-2}$ and $4.76 \times 10^{14} \text{ molec cm}^{-2}$ respectively, both reaching their maximum in March and their minimum in September, due to the tropopause height variation. Further, HNO₃ and HCl data were used to compare with Microwave Limb Sounder (MLS) satellite data. MLS satellite data showed similar seasonal variations and annual rates with FTIR data, and the stratospheric HNO₃ and HCl columns of the two datasets have correlation coefficients (r) of 0.87 and 0.88, respectively. The mean bias between satellite and FTIR data of stratospheric HNO₃ and HCl columns are $(-8.58 \pm 12.22)\%$ and $(4.58 \pm 13.09)\%$, respectively.

Keywords: FTIR; ground based remote sensing; HNO₃; HCl; stratospheric column



Citation: Shan, C.; Zhang, H.; Wang, W.; Liu, C.; Xie, Y.; Hu, Q.; Jones, N. Retrieval of Stratospheric HNO₃ and HCl Based on Ground-Based High-Resolution Fourier Transform Spectroscopy. *Remote Sens.* **2021**, *13*, 2159. <https://doi.org/10.3390/rs13112159>

Academic Editors: Filomena Romano and Elisabetta Ricciardelli

Received: 7 April 2021

Accepted: 28 May 2021

Published: 31 May 2021

Publisher's Note: MDPI stays neutral with regard to jurisdictional claims in published maps and institutional affiliations.



Copyright: © 2021 by the authors. Licensee MDPI, Basel, Switzerland. This article is an open access article distributed under the terms and conditions of the Creative Commons Attribution (CC BY) license (<https://creativecommons.org/licenses/by/4.0/>).

1. Introduction

Nitric acid (HNO₃) is one of the main reservoirs of stratospheric odd nitrogen species (NO_y = NO + NO₂ + HNO₃ + HO₂ + NO₂ + 2N₂O₅ + ClONO₂ + trace components), and NO_x (NO and NO₂) [1]. In the stratosphere, NO_x can catalytically destroy O₃, so HNO₃ indirectly participates in the process of O₃ depletion [2]. HNO₃ is an important component of the formation of polar stratospheric clouds (PSCs). The PSCs can provide a reaction surface for heterogeneous reactions, converting inactive chlorine and bromine into active forms, leading to the stratospheric O₃ depletion in polar regions [3]. Furthermore, HNO₃ is mainly produced by OH• radicals and NO₂ in the daytime under the catalysis of third intermediates and dissociated by the reaction with OH• or photolysis in the daytime [4].

In the stratosphere, other catalysts that lead to the depletion of ozone are active chlorine species (Cl• and ClO•), while the hydrogen chloride species (HCl) is the primary constituent of inorganic chlorine and one of the most important chlorine reservoirs in the stratosphere [5–8]. Atmospheric HCl is formed by the reaction of the Cl• radical from CFCs photolysis, with hydrocarbons (RH•) [6,9]. The chlorine reservoir is converted to

active chlorine that destroys ozone on polar stratospheric clouds (PSCs) or cold binary sulfate aerosol through heterogeneous reactions [10–12].

HNO₃ and HCl have been measured by many methods and techniques. Airborne or balloon-borne in-situ measurements with high accuracy and precision have been performed to detect HNO₃ and HCl concentrations and vertical profiles, but the measurements are easily affected by vertical air-mass transport [13–17]. The global temporal and spatial distributions of HNO₃ and HCl can be obtained by satellite remote sensing instruments, such as the Infrared Atmospheric Sounding Interferometer (IASI on MetOp satellite), the Atmospheric Chemistry Experiment-Fourier Transform Spectrometer (ACE-FTS on SCISAT), the Microwave Limb Sounder (MLS carried on Aura), and the Michelson Interferometer for Passive Atmospheric Sounding (MIPAS) [18–23]. However, satellite data show high measurement error and low sensitivity for near-surface observations. The ground-based FTIR technique detects the long-term trend of trace gases in the atmosphere with high precision and accuracy, and the measurements are not affected by vertical air-mass transport [24,25]. FTIR measurements are often used to analyze the long-term trends, seasonal variabilities of trace gases and to validate in-situ and satellite measurements [22,26]. Total column and vertical profiles of HNO₃ and HCl were obtained by ground-based FTIR over the past decade [18,27–29]. Rinsland (1991) obtained a long-term time series of atmospheric HNO₃ total columns at mid-latitudes using ground-based FTIR, and compared the data with the values reported in other studies for mid-latitude [30]. These measurements are often used to identify polar intrusion events and monitor chlorine species during the ozone hole period [31,32].

This study utilizes high resolution mid-infrared solar spectra collected by ground-based FTIR, to retrieve vertical profiles of HNO₃ and HCl and stratospheric columns. The outline of the paper is as follows. We describe the HNO₃ and HCl measurement site and instrument, the retrieval method and the error analysis in Section 2. In Section 3, the spatial-temporal distribution and seasonal variability of stratospheric HNO₃ and HCl are discussed. Because the DOFs of the profiles are low, we focus on the analyses of the stratospheric columns based on the profiles. The vertical profiles and stratospheric HNO₃ and HCl columns obtained from FTIR and the Aura/MLS satellite (NASA, USA) are compared in Section 4. Section 5 summarizes our findings and gives our conclusions.

2. Retrieval of Atmospheric HNO₃ and HCl

2.1. Measurement Site and Instrument

The observation site (31.540° N, 117.100° E, 29 m a.s.l.), adjacent to a reservoir named DongPu, is located in the north-west of Hefei city in eastern China. We installed the ground-based remote sensing system Figure 1, consisting of a high-resolution FTIR instrument (Bruker IFS 125HR) and a solar tracker (A547N), to monitor the atmospheric trace gas since 2014. A meteorological station (ZENO, Coastal Environmental Systems, USA) on the roof of the lab building, has recorded meteorological data since September 2015 [33,34].

The FTIR instrument collects near-infrared and mid-infrared solar absorption spectra alternately on clear days. The FTIR instrument, equipped with a Potassium bromide (KBr) beamsplitter and an indium antimonide (InSb) detector along with a mercury cadmium telluride (MCT) detector, collects mid-infrared spectra (600–4500 cm⁻¹) with a spectral resolution of 0.005 cm⁻¹. The instrument line shape (ILS) of the FTIR instrument is monitored by low-pressure HCl and HBr cell measurement to maintain good alignment of the FTIR instrument [34–36].

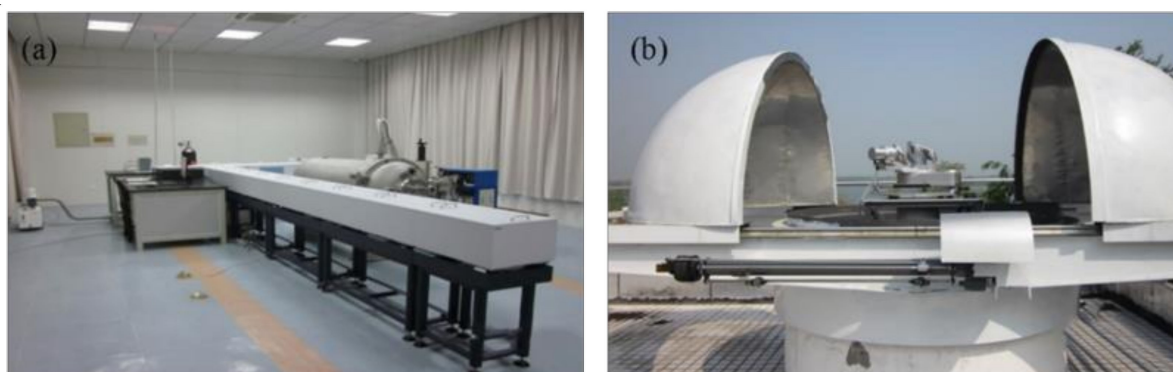


Figure 1. The FTIR instrument system at Hefei site: (a) Bruker 125HR Fourier transform infrared spectrometer; (b) solar tracker.

2.2. Retrieval Method

The SFIT4 (version 0.9.4.4) retrieval algorithm is adopted to retrieve the vertical profiles of HNO₃ and HCl from the solar absorption spectra. The retrieval algorithm is based on the optimal estimation method (OEM) [37]. The relationship between the measurement vector y and the atmospheric state vector x is expressed as follows:

$$y = F(x, b) + \varepsilon \quad (1)$$

where x represents the quantities to be retrieved, b is the parameters affecting the measurement, ε represents measurement noise, and F is a forward model function that describes the entire physical process of the measurement. The retrieval algorithm finds the state vector \hat{x} close to the true state vector x based on the measured quantity y :

$$x_{i+1} = x_a + S_c K_i^T (K_i S_c K_i^T + S_a)^{-1} (y - F(x_i, b) + K_i (x_i - x_a)) \quad (2)$$

$$\hat{x} = x + (A - I)(x - x_a) + G_y K_b (b - b_r) + G_y (y - y_r) \quad (3)$$

$$A = (K^T S_c^{-1} K + S_a^{-1})^{-1} K^T S_c^{-1} K \quad (4)$$

where K_i is the weight function matrix of the i -th iteration, and $K_i = \frac{\partial F}{\partial x}$. The quantity x_a is the a priori state vector, which includes the profile of the atmosphere state and instrument parameter, S_a and S_c are the a priori and measurement error covariance matrix, respectively, and \hat{x} is the inversion profile. I is the identity matrix, G_y is the gain matrix, K_b is the sensitivity matrix of b , b_r is the estimate model parameter, and y_r is the simulated measurement state vector after inversion [37]. The averaging kernel matrix A represents the sensitivity and the vertical smoothing extent of the retrieved data. The retrieved state ($\hat{x} - x_a$) is calculated from the estimate of the true state obtained from the measurement ($x - x_a$) and the averaging kernel [37,38]:

$$\hat{x} - x_a = A(x - x_a) \quad (5)$$

The a priori profiles of target gases and interfering gases except H₂O and HDO are adopted from the Whole Atmosphere Community Climate Model (WACCAM). The daily temperature, pressure, and H₂O and HDO profiles are obtained from the reanalysis data of the National Center for Environmental Prediction (NCEP). Spectroscopic line parameters are adopted from the HITRAN 2008 database and its updates [39,40]. A set of spectral micro-windows for HNO₃ and HCl are chosen to retrieve the concentration of the two gases by considering the minimum absorption of water vapor (H₂O) and other interfering species. There are two micro-windows (MW) for HNO₃ retrieval with the wavenumber region centered in 869 and 872 cm⁻¹. There are three micro-windows for HCl retrieval

centered at 2727.70, 2775.75 and 2925.85 cm^{-1} . These micro-windows are often used in the retrieval of satellite data and FTIR data at other sites [22,27,41]. The specific parameter settings for HNO_3 and HCl retrieval are shown in Table 1. In addition to HNO_3 and HCl , the spectroscopic signatures of interfering gases are also considered to reduce fitting residuals. H_2O and HDO are treated as two different species for retrieval.

Table 1. HNO_3 and HCl retrieval parameter settings. MW is the abbreviation of micro-window.

Species	HNO_3		HCl	
Retrieval algorithm	SFIT4 0.9.4.4		SFIT4 0.9.4.4	
Atmospheric stratification	48 layers		48 layers	
Simulated height	0–120 km		0–120 km	
Spectra resolution	0.005 cm^{-1}		0.005 cm^{-1}	
Spectroscopic line parameters	HITRAN 2012		HITRAN 2012	
T, P and H_2O profiles	NCEP		NCEP	
A priori profiles of retrieved species	WACCAM		WACCAM	
Spectral range (cm^{-1})	MW1	868.47–870.00	MW1	2727.68–2727.82
	MW2	872.80–874.00	MW2	2775.60–2775.90
			MW3	2925.65–2926.10
Interfering species	MW1	$\text{H}_2\text{O}, \text{OCS}, \text{NH}_3, \text{CO}_2$	MW1	$\text{O}_3, \text{H}_2\text{O}, \text{HDO}$
	MW2	$\text{H}_2\text{O}, \text{OCS}, \text{NH}_3, \text{CO}_2$	MW2	$\text{O}_3, \text{H}_2\text{O}, \text{N}_2\text{O}$
			MW3	CH_4, NO_2

2.3. Error Analysis

Error analysis is based on the posterior error estimation method of Rodgers [37]. The error sources for HNO_3 and HCl error estimation, such as the temperature profile, solar zenith angle (SZA), spectroscopic line parameters, interfering species, and their uncertainties are listed in Table 2. The results of error analysis for a typical HNO_3 and HCl retrieval (measured at 01:51 UTC on 10 February 2017, with SZA of 58.76°) are summarized in Table 3. The total errors for HNO_3 and HCl are about 12.16% and 10.09%, respectively, based on the combination of random and systematic errors. The total error for HNO_3 is 13.5% in the Eureka site [42]. The error profile of HCl and HNO_3 are plotted in the Appendix A Figures A1 and A2, respectively. For HNO_3 , the dominating random errors are the smoothing error and the measurement noise, with an error of 7.86%. As for the systematic error, it amounts to an error of 9.28%, dominated by errors from spectroscopic line parameters. For HCl , the random error is mainly from smoothing error and zero level shift, with an error of 1.47%. The systematic error is dominated by errors from spectroscopic line parameters, with an error of 9.98%. It is clear that uncertainties of the line intensity parameter for the HNO_3 and HCl absorption lines and smoothing error are the main error sources for their retrieval.

Table 2. Random and systematic uncertainties used in the error estimation.

Parameter	Random Uncertainty	Systematic Uncertainty
Temperature	2K troposphere 5K stratosphere	2K troposphere 5K stratosphere
Solar line shift	0.005 cm^{-1}	0.005 cm^{-1}
Solar zenith angle	0.025°	0.025°
Solar line strength	0.1%	0.1%
Phase	0.001 rad	0.001 rad
Zero level shift	0.01	0.01
Wavenumber shift	0.001 cm^{-1}	0.001 cm^{-1}
Background slope	0.001 cm^{-1}	0.001 cm^{-1}

Table 2. Cont.

Parameter	Random Uncertainty	Systematic Uncertainty
Background curvature	0.001 cm ⁻¹	0.001 cm ⁻¹
Field of view	0.001	0.001
Line intensity	/	10.0%
Line T broadening	/	10.0%
Line P broadening	/	10.0%
Interfering species	2% (H ₂ O profile)	2% (H ₂ O profile)

Table 3. Mean random and systematic errors for HNO₃ and HCl retrieval.

	HNO ₃		HCl	
	Random Error/%	Systematic Error/%	Random Error/%	Systematic Error/%
Smoothing error	5.08	/	2.09	/
Measurement error	3.26	/	0.67	/
Retrieval error	0.05	/	0.01	/
Interfering species	0.20	/	0.05	/
Temperature	1.61	2.22	0.74	1.73
Solar zenith angle	0.07	0.07	0.05	0.05
Zero level shift	0.82	0.82	1.04	1.04
Background curvature	0.50	0.50	/	/
Phase	0.01	0.01	0.15	0.12
Line intensity	/	8.76	/	7.52
Subtotal error	7.86	9.28	1.47	9.98
Total error		12.16		10.09

3. Results and Discussion

Vertical Distributions of HNO₃ and HCl

Figure 2 presents the measured HNO₃ and HCl profiles and a priori profiles during the observation period from January 2017 to December 2019 at the Hefei site. As shown in Figure 2, the concentrations of HNO₃ and HCl are small and very close to the a priori profile below the tropopause, and both stratospheric concentrations are higher than those in troposphere. HNO₃ mostly exists at heights of 20–30 km (Figure 2a), and HCl mainly exists at heights of 30–50 km (Figure 2b). While the shape of the retrieved HNO₃ profile is similar to that of the a priori profile, and the measured profiles have a relatively small variation between 15 and 30 km.

Figure 3 displays typical HNO₃ and HCl averaging kernels and sensitivity at the Hefei site, which depicts the sensitivity of height dependence of the retrieved profile to concentration perturbations at the various atmospheric levels. Also shown in Figure 3 is the retrieval sensitivity, which is calculated as the sum of the corresponding averaging kernel at each layer j ($\sum_j A_{ij}$, with A the averaging kernels matrix). The sensitivity represents the fraction of the retrieval that comes from the measurement rather than from the a priori profile [22]. In Figure 3, the averaging kernels are close to zero in the atmosphere below 10 km and above 40 km, which means that the sensitivity of HNO₃ measurements is very low. For HCl, the height region with the averaging kernels close to zero are below 10 km and above 50 km. It is found that the most sensitive height range for HNO₃ and HCl are at 20–30 km. The trace of the averaging kernel matrix gives the degrees of freedom for signal (DOFs), which represent the number of independent pieces of information in the profile. The typical cumulative sum of DOFs profile for HNO₃ and HCl are shown in Figure 3b,d. The typical DOFs for HNO₃ retrieval at the Hefei site are 1.3 ± 0.13 , and the main contribution is from the stratosphere (83%, 16–41 km), with the DOFs of 1.08 ± 0.06 . The typical DOFs of HCl are 2.12 ± 0.23 , and the DOFs from the stratosphere are 1.63 ± 0.23 . As shown in Figure 3, the contribution of DOFs below 12 km and above 41 km are small for HNO₃ and HCl. Therefore, we focus on the stratospheric partial columns of HNO₃

and HCl at the Hefei site. The stratospheric partial column is computed by integrating the retrieved profiles of HNO₃ and HCl for the height region from 12 km to 41 km.

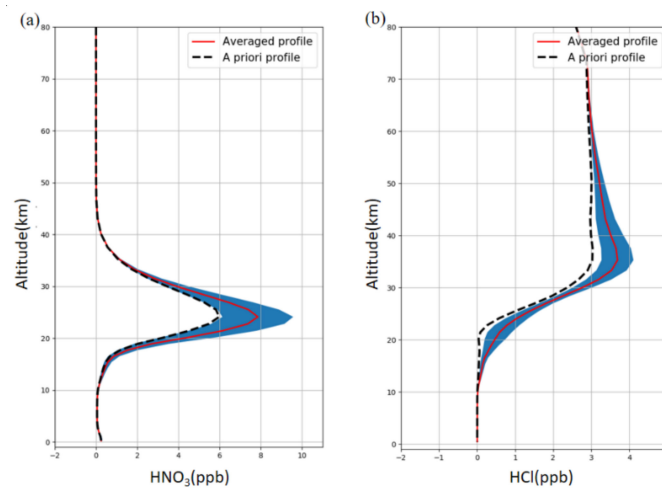


Figure 2. Measured HNO₃ and HCl profiles and a priori profiles during the observation period from January 2017 to December 2019 at the Hefei site. Panel (a,b) represent the HNO₃ and HCl averaged retrieved profile (red line) and a priori profile (black dot line), the blue shade region is the 1- σ standard deviation.

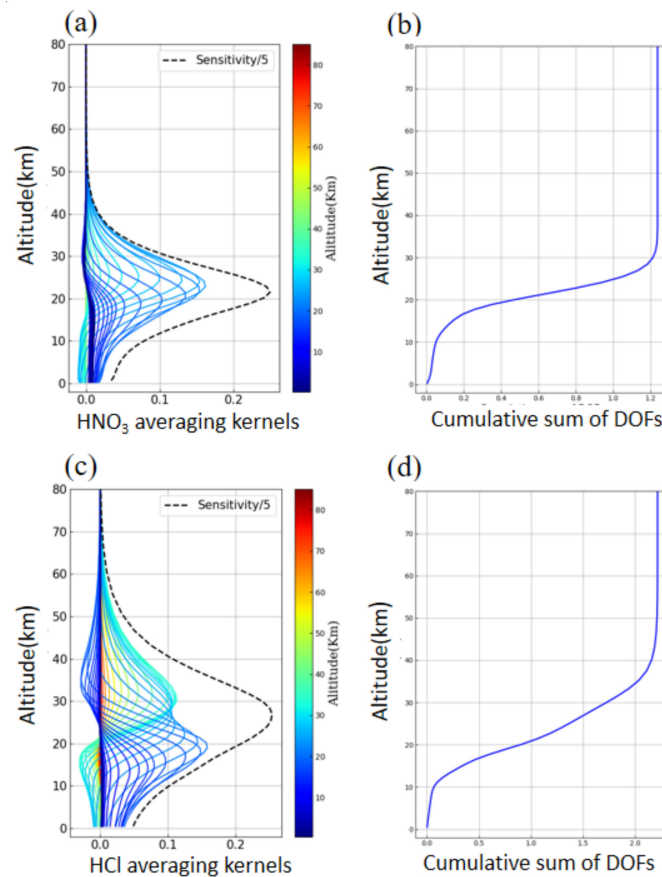


Figure 3. The typical averaging kernel matrix and DOFs distribution of HNO₃ and HCl. (a,c) are the averaging kernel for HNO₃ and HCl, sensitivity plotted with the dash line; (b,d) are the DOFs distribution of HNO₃ and HCl. The spectrum is collected at 01:51 UTC (SZA 58.76°), 10 February 2017 in Hefei, China.3.2. Time Series of Stratospheric HNO₃ and HCl.

The individual and daily averaged stratospheric partial columns of HNO_3 and HCl measured from January 2017 to December 2019 over Hefei are shown in Figure 4. The time series were fitted by a lowpass filtering fast Fourier transform (FFT) technique in order to reveal the seasonal and interannual variation of stratospheric HNO_3 and HCl at the Hefei site [43]. In the FFT fitting, the cutoff frequencies of 2-years and 90-days were used to calculate the long-term trend and seasonal variations, respectively. The time series of stratospheric HNO_3 and HCl show an obvious annual decreasing trend and seasonal variation. The annual decreasing rate of stratospheric HNO_3 and HCl is $(9.45 \pm 1.20)\% \text{ yr}^{-1}$ and $(7.04 \pm 0.81)\% \text{ yr}^{-1}$, respectively. Satellite observations also give a decreasing trend for the total column HNO_3 (at $30\text{--}40^\circ\text{N}$) and HCl (at $45\text{--}50^\circ\text{N}$) [23,44]. Kohlhepp (2012) obtained total column of HCl with trends that ranged from -4 to -16% decade $^{-1}$ from 17 NDACC stations for the years 2000 to 2009 [45]. The annual decreasing trend for stratospheric HNO_3 , that is formed in the upper part of the stratosphere through photo dissociation of oxygen and nitrogen and further oxidation of NO and NO_2 to HNO_3 , underlies a middle atmosphere circulation effect [46,47]. Similarly, the decreasing emission of CFCs, the precursors of HCl , due to a long term regulation process—internationally, reduced the stratosphere HCl concentrations [48,49]. Also, oxidation with the hydroxyl radical and photo-dissociation degrade stratospheric HNO_3 and HCl [31].

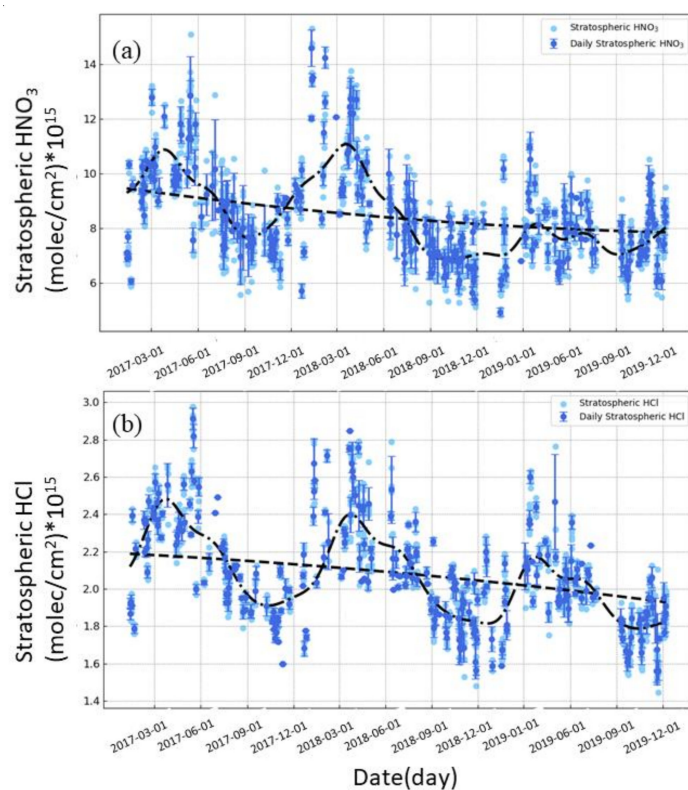


Figure 4. HNO_3 and HCl seasonality at the Hefei site: (a) time series of stratospheric partial column of HNO_3 , (b) time series of stratospheric partial column of HCl . The light blue dots are the individual measurements of HNO_3 and HCl , the blue dots represents the daily averaged HNO_3 and HCl ; the error bars are standard deviations of the daily averaged HNO_3 and HCl , the black line is the fitting curve.

The HNO_3 seasonality was captured at the Hefei site as shown in Figure 4a. To clearly show the seasonal variation, we de-trended the stratospheric HNO_3 by subtracting the long-term trends. The de-trended daily and monthly averaged HNO_3 are shown in Figure 5a. The peak value of stratospheric HNO_3 appears in March, and then decreases to a minimum in September over the three years of measurement. The monthly averaged seasonal amplitude of stratospheric HNO_3 is $2.67 \times 10^{15} \text{ molec/cm}^2$. The de-trended

stratospheric HCl is shown in Figure 5b. Similar to the seasonal variation of HNO_3 , the maximum partial column of HCl appeared in March and the minimum was in September, during the three years of measurement. The monthly averaged seasonal amplitude of stratospheric HCl is 4.76×10^{14} (molec/cm^2).

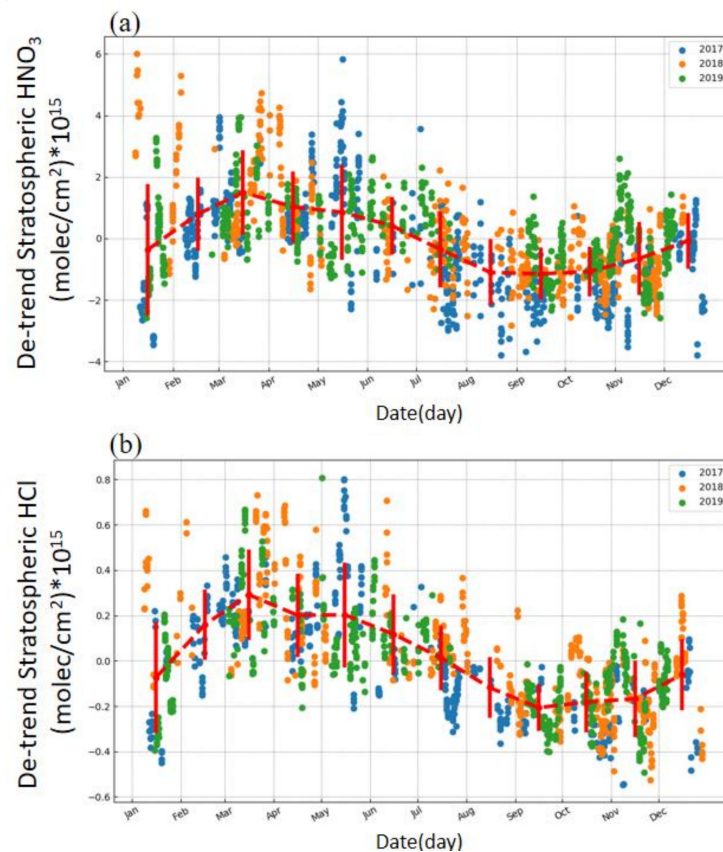


Figure 5. De-trended stratospheric partial columns of HNO_3 and HCl from 2017 to 2019. (a) the de-trended stratospheric partial columns of HNO_3 , and (b) the de-trended stratospheric partial columns of HCl. The error bars are standard deviations of monthly averaged HNO_3 and HCl.

The seasonal variation of stratospheric columns of HNO_3 and HCl are mainly associated with tropopause height variation. The seasonal variation of tropopause height calculated from the NCEP reanalysis data over Hefei are given in Figure 6. As shown in Figure 6, the tropopause height was highest in February and March, and lowest in July, August and September. It seems that the higher the tropopause height, the smaller the stratospheric columns abundance of HNO_3 and HCl. Further, the relationship of the monthly averaged de-trended stratospheric HNO_3 and HCl and the monthly averaged tropopause height are plotted in Figure 7. The correlation coefficient is -0.67 and -0.59 for HNO_3 and HCl, respectively. The seasonal variation of the tropopause results from stratospheric general circulation transporting air from the summer to the winter hemisphere [44,50,51]. When the tropopause rises in summer, the partial columns of trace gases in the stratosphere often transport to colder areas, thus the stratospheric HNO_3 and HCl columns are lower during this period [44]. In addition, the strong solar radiation enhances the photolysis of stratospheric HNO_3 and HCl with OH in summer, which also explains the low concentrations of HNO_3 and HCl in the stratosphere [44,52,53].

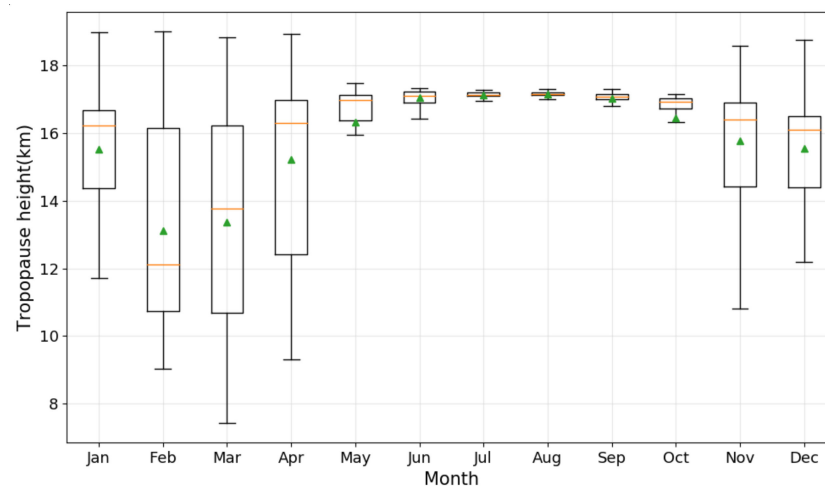


Figure 6. Box plot of the monthly tropopause height distribution calculated from the NCEP reanalysis data from 2017 to 2019 at Hefei site. The yellow line is the middle value of the monthly dataset, the top and bottom of box are the third and first quartile of the monthly dataset. The error bar is the maximum and minimum of the monthly dataset. Green dots are the monthly averaged tropopause height.

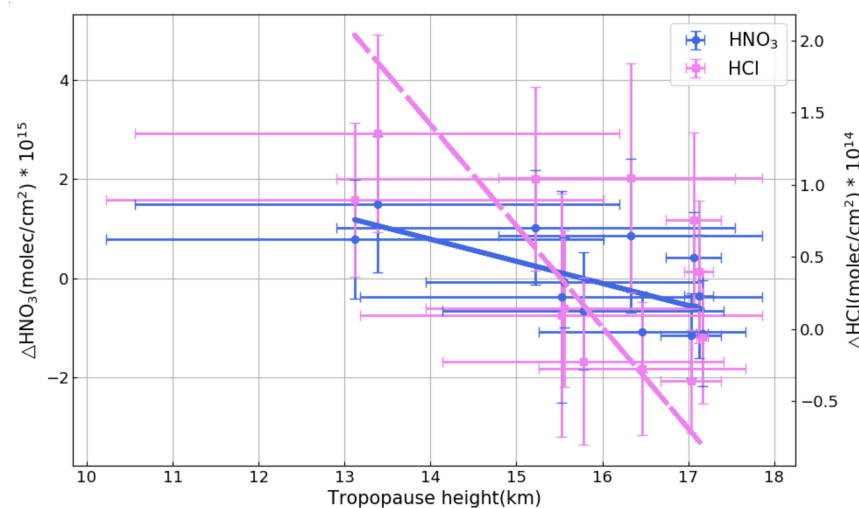


Figure 7. The relationship of monthly averaged de-trend stratospheric columns of HNO_3 and HCl with monthly averaged tropopause height at the Hefei site during the observations. The blue lines represent the relationship of de-trend stratospheric HNO_3 with tropopause height, and the magenta dash lines represent the relationship of de-trend stratospheric HCl with tropopause height.

4. Comparison with Satellite Data

The MLS on the Aura satellite was launched on 15 July 2004 to monitor atmospheric trace species from the upper troposphere to the mesosphere [54]. The orbit of MLS is sun-synchronous, located at 705 km altitude, and vertical profiles are measured every ~ 165 km along the suborbital track [55]. The HNO_3 and HCl satellite data are MLS version 4.2 [56,57]. The collocation criteria for selecting a comparison dataset are differences in locations with MLS data within $\pm 3^\circ$ radius of the Hefei site and differences in time between FTIR measurements and satellite overpass within ± 2 h.

It is difficult to directly compare the raw profiles observed from MLS with FTIR data due to the difference in vertical sensitivity of the two measurements [37]. In order to reduce the impact of the different averaging kernels, we use the method of Rodgers and Connor (2003) to smooth the profiles observed by the satellite [37], that is:

$$x_{corr} = x_{fp} + A(x_{sat} - x_{fp}) \quad (6)$$

where x_{sat} is the raw profile of the satellite, x_{fp} is the a priori profile of FTIR observations, A is the FTIR averaging kernels matrix, and x_{corr} is the smoothed profile of the satellite. The raw and smoothed satellite profiles of HNO₃ and HCl are shown in Figure 8, the green shade and orange shade represent the smoothed and raw data uncertainty, respectively. After smoothing, the profiles of HNO₃ and HCl show low uncertainty compared to the raw data. Despite the similar shape of the HNO₃ profiles observed by satellite and FTIR, the satellite observations have lower HNO₃ concentrations, especially at the height from 23 to 30 km. This difference in the profile shape of HNO₃ was also reported between the IASI satellite and FTIR data [22]. The satellite data show that the concentrations of HNO₃ are greater than FTIR data between 17 and 25 km, and lower than FTIR data above 25 km for HCl.

Next is the comparison of the stratospheric partial column for satellite and FTIR data. The stratospheric partial columns of HNO₃ and HCl observed by satellite are obtained by integrating the profiles of HNO₃ and HCl from 12 to 41 km. The relative difference between the stratospheric partial columns obtained from the FTIR and the smoothed satellite data are calculated as follows:

$$r(\%) = \frac{PC_{FTIR} - PC_{satellite}}{PC_{FTIR}} \times 100 \quad (7)$$

where r represents the relative difference of the two data, PC_{FTIR} and $PC_{satellite}$ are stratospheric partial columns obtained from FTIR and satellite, respectively.

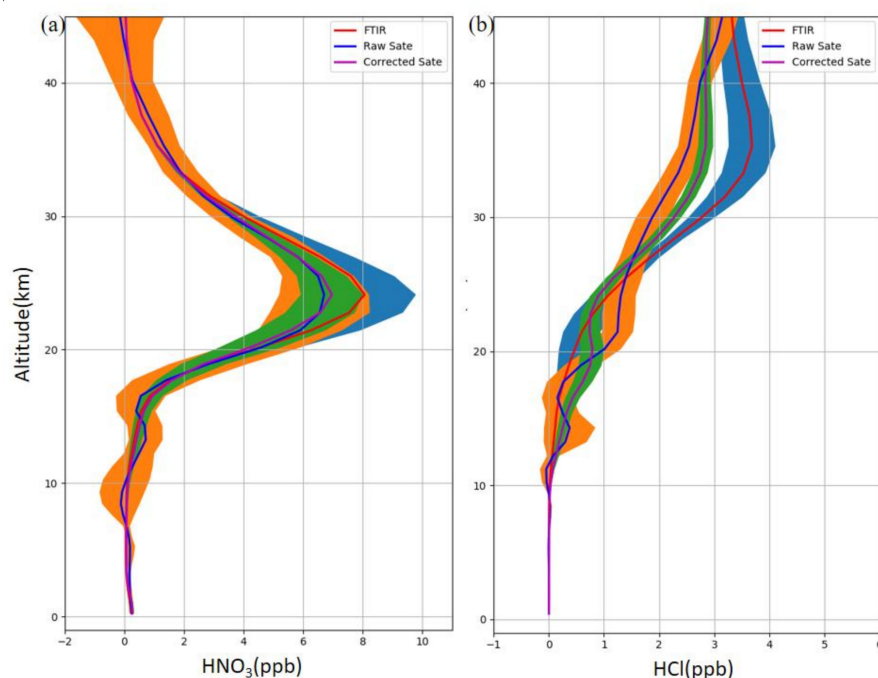


Figure 8. Raw and smoothed profiles of (a) HNO₃ and (b) HCl observed by satellite with FTIR data. The shade area represents the standard deviation of averaged HNO₃ and HCl for FTIR (in blue) and for MLS satellite data (in orange: raw data; in green: smoothed data).

The individual and daily averaged co-located stratospheric HNO₃ and HCl columns obtained by FTIR and satellite are presented in Figure 9. Stratospheric columns of HNO₃ and HCl from the satellite are in good agreement with the coincident FTIR data. Further, Figure 10 shows high correlation between FTIR and satellite data, with the correlation coefficient (r) of 0.87 and 0.88 for daily averaged HNO₃ and HCl, respectively. For HNO₃ and HCl, a decreasing annual rate of $(-8.73 \pm 1.32)\%$ and $(-6.52 \pm 1.07)\%$ respectively are derived from the satellite data, and both values are slightly lower than the corresponding data from FTIR. The seasonal variations of satellite data are similar to the FTIR data,

with the maximum and minimum of HNO_3 and HCl in March and September, respectively. The averaged seasonal amplitude of HNO_3 and HCl is $2.46 \times 10^{15} \text{ molec cm}^{-2}$ and $4.69 \times 10^{14} \text{ molec/cm}^{-2}$ for satellite data, similar to those from FTIR data.

The statistics of the comparison results are listed in Table 4, showing the bias and correlation between FTIR and satellite data in each year. The mean bias (satellite data minus FTIR data) of HNO_3 and HCl between FTIR and satellite data are $(8.58 \pm 12.22)\%$ and $(-4.58 \pm 13.09)\%$, respectively. The bias is largely attributed to the following factors: the grid and observation times of the satellite data are not exactly the same as those of FTIR observations, and there is a difference in the a priori profiles between FTIR and satellite data. Additionally, the seasonality of the residual is mostly due to the solar zenith angle variation of the measurements and the a priori profile difference of two instruments [58]. Fu (2011) compared the stratospheric partial columns of HNO_3 and HCl measured by ground-based FTIR (GB-FTIR) with the space-borne ACE-FTS data products [41]. The results showed that the average difference for the two data were -6.6% and -8.5% for HNO_3 and HCl , respectively.

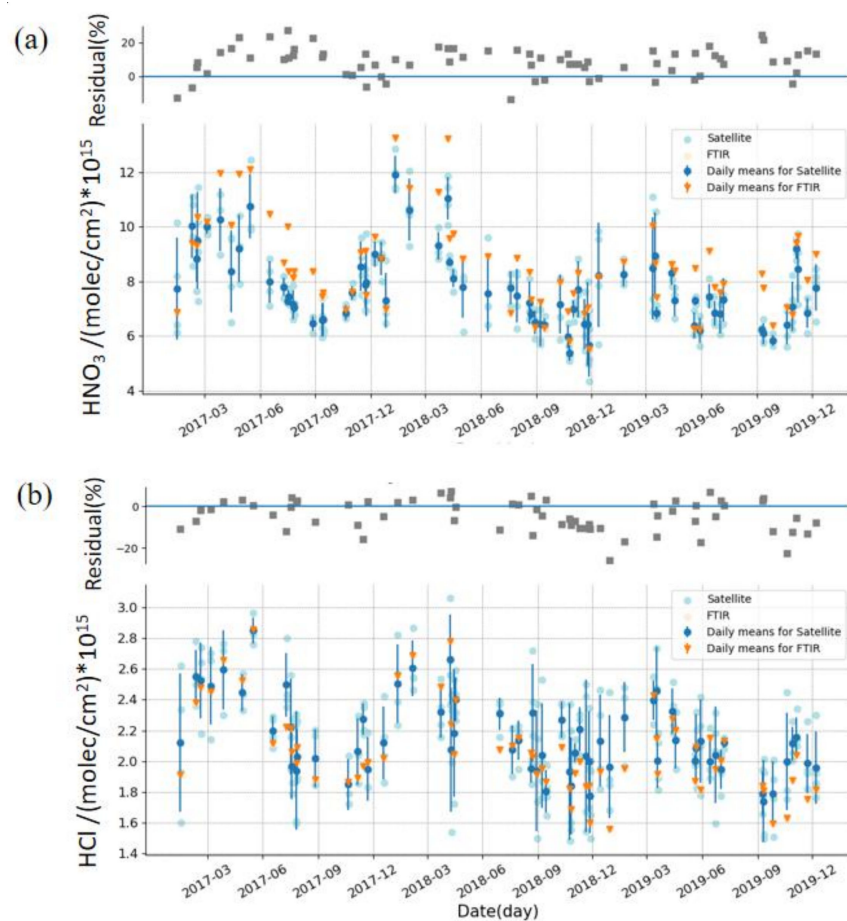


Figure 9. Comparison of (a) HNO_3 and (b) HCl partial columns in the stratosphere observed by GB-FTIR (red dots) with those observed by MLS satellite (blue dots). The upper panels of (a,b) are residual results for FTIR data and satellite data.

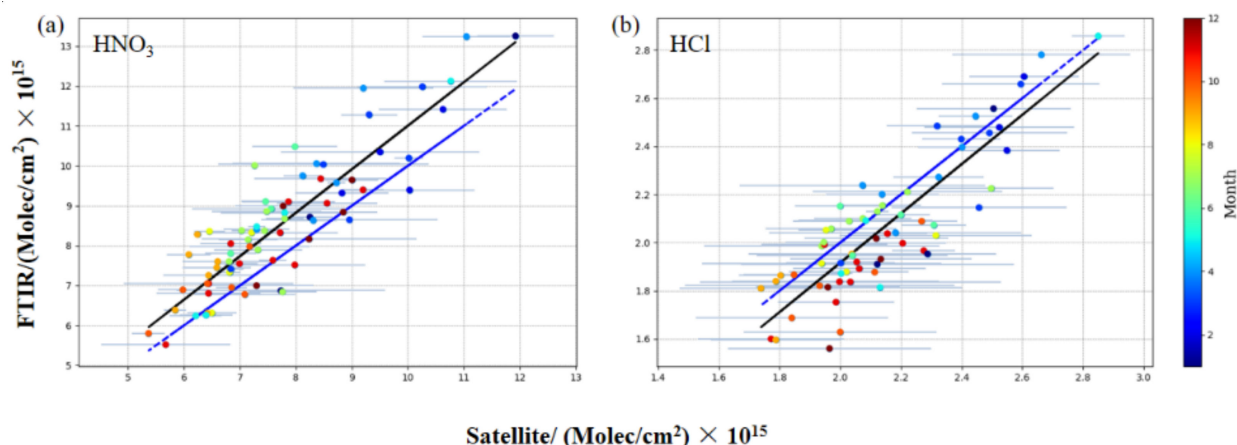


Figure 10. Scatter plots of (a) HNO₃ and (b) HCl partial columns in the stratosphere, observed by GB-FTIR and MLS satellite from 2017 to 2019. The black lines represent the correlation fitting curves and blue line is $y = x$.

Table 4. Results of comparison between HNO₃ and HCl partial column in the stratosphere, measured by FTIR and the MLS satellite from 2017 to 2019.

Species	Year	Coincident Pairs	Mean Relative Difference	Correlation Coefficient
HNO ₃	2017	98	$(8.39 \pm 13.45)\%$	0.64
	2018	91	$(7.99 \pm 12.14)\%$	0.87
	2019	83	$(9.44 \pm 10.63)\%$	0.67
	Total	272	$(8.58 \pm 12.22)\%$	0.78
HCl	2017	70	$(-3.22 \pm 11.31)\%$	0.73
	2018	94	$(-4.49 \pm 14.62)\%$	0.63
	2019	79	$(-5.9 \pm 12.49)\%$	0.65
	Total	243	$(-4.58 \pm 13.09)\%$	0.71

5. Conclusions

In this study, we present stratospheric columns of HNO₃ and HCl retrieved by ground-based high resolution FTIR remote sensing measurements. The stratospheric columns of HNO₃ and HCl were retrieved from mid-infrared solar absorption spectra based on the optimal evaluation algorithm, SFIT4.

The time series of stratospheric columns of HNO₃ and HCl over Hefei during January 2017 to December 2019 are presented, and compared with MLS satellite data. Stratospheric HNO₃ and HCl showed a decreasing rate of $(9.45 \pm 1.20)\% \text{ yr}^{-1}$ and $(7.04 \pm 0.81)\% \text{ yr}^{-1}$ respectively during the observation period. The decreasing annual trend for stratospheric HNO₃ and HCl is due to the reduction of their precursor, NO_x and CFCs in the stratosphere. Stratospheric HNO₃ and HCl peaked in March and reached the lowest value in September, with seasonal amplitudes of $2.67 \times 10^{15} \text{ molec cm}^{-2}$ and $4.76 \times 10^{14} \text{ molec cm}^{-2}$, respectively.

We also use FTIR data to evaluate the performance of MLS data for observation of HNO₃ and HCl. The HNO₃ profiles observed by MLS satellite have similar shapes as those measured by FTIR, but the MLS data concentrations are less than the concentrations of HNO₃. For HCl, the concentrations observed by MLS are higher than the FTIR data between 17 and 25 km, but smaller than the FTIR data above 25 km. The MLS data have a similar seasonal variation and inter-annual trend as those of the FTIR observations, and the correlation coefficient (r) between the two data is 0.87 and 0.88 for HNO₃ and HCl, respectively. The maximum and minimum HNO₃ and HCl stratospheric columns observed by MLS satellite occur in March and September, with the seasonal amplitude of $2.46 \times 10^{15} \text{ molec cm}^{-2}$ and $4.69 \times 10^{14} \text{ molec cm}^{-2}$. The mean bias between FTIR and the satellite data for stratospheric HNO₃ and HCl are $(8.58 \pm 12.22)\%$ and $(-4.58 \pm 13.09)\%$, respectively.

Author Contributions: Funding acquisition, W.W., C.L. and Q.H.; resources, Y.X.; supervision, N.J.; writing—original draft, C.S. and H.Z.; writing—review and editing, W.W. All authors have read and agreed to the published version of the manuscript.

Funding: We gratefully acknowledge the support of the National Natural Science Foundation of China (41775025, 41722501, 91544212, 51778596, 41575021 and 41977184), the National Key Technology R&D Program of China (2018YFC0213201, 2019YFC0214702, 2016YFC0200404, 2017YFC0210002, 2018YFC0213104, and 2019YFC0214802), the Major Projects of High Resolution Earth Observation Systems of National Science and Technology (05-Y30B01-9001-19/20-3), the Strategic Priority Research Program of the Chinese Academy of Sciences (XDA23020301), the National Key Project for Causes and Control of Heavy Air Pollution (DQGG0102 and DQGG0205), the Natural Science Foundation of Guangdong Province (2016A030310115), the project supported by the Presidential Foundation of the Hefei Institutes of Physical Science, Chinese Academy Sciences, China-“Spark” (No. YZJJ2021QN06), and funded by the Research Fund Program of Guangdong-Hongkong-Macau Joint Laboratory of Collaborative Innovation for Environmental Quality (GHML2021-102).

Institutional Review Board Statement: Not applicable.

Informed Consent Statement: Not applicable.

Data Availability Statement: The data presented in this study are available on request from the corresponding author.

Acknowledgments: The processing environment of SFIT4 and some plot programs are provided by the National Center for Atmospheric Research (NCAR), Boulder, Colorado, USA. The NDACC networks is acknowledged for supplying the SFIT software and advice.

Conflicts of Interest: The authors declare no conflict of interest.

Appendix A

The square root of the diagonal elements of the error covariance matrices of HCL and HNO₃, for a typical measurement spectrum (measured at 01:51 UTC on 10 February 2017, with SZA of 58.76°), are depicted in Figures A1 and A2. The vertical structures of the error profiles reflect the effect of the propagation of different errors in the retrieval.

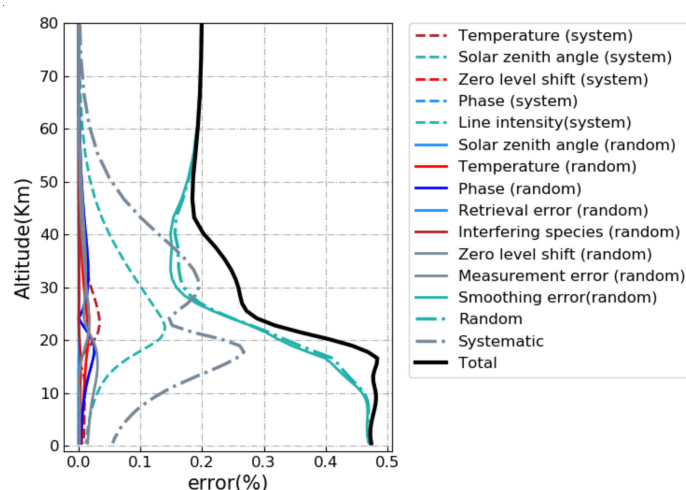


Figure A1. Errors in the retrieved HCl due to the uncertainties as listed in Table 2.

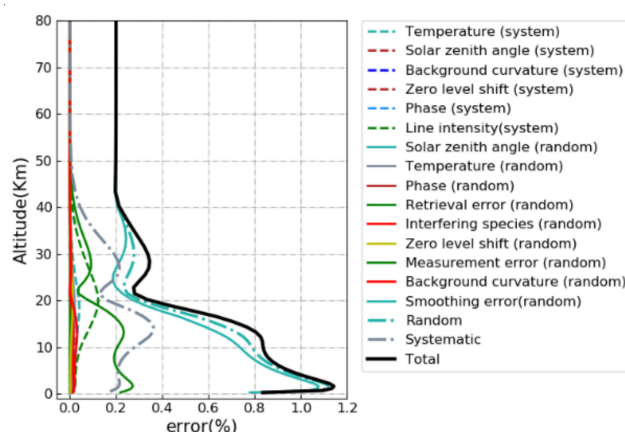


Figure A2. Errors in the retrieved HNO₃ due to the uncertainties as listed in Table 2.

References

- Wood, S.W.; Batchelor, R.L.; Goldman, A.; Rinsland, C.P.; Connor, B.J.; Murcray, F.J.; Stephen, T.M.; Heuff, D.N. Ground-based nitric acid measurements at Arrival Heights, Antarctica, using solar and lunar Fourier transform infrared observations. *J. Geophys. Res.* **2004**, *109*, D18307. [[CrossRef](#)]
- Solomon, S.; Ivy, D.J.; Kinnison, D.; Mills, M.J.; Neely, R.R.; Schmidt, A. Emergence of healing in the Antarctic ozone layer. *Science* **2016**, *353*, 269–274. [[CrossRef](#)] [[PubMed](#)]
- Zhu, Y.; Toon, O.B.; Kinnison, D.; Harvey, V.L.; Mills, M.J.; Bardeen, C.G.; Pitts, M.; Bègue, N.; Renard, J.-P.; Berthet, G.; et al. Stratospheric aerosols, polar stratospheric clouds, and polar ozone depletion after the Mount Calbuco eruption in 2015. *J. Geophys. Res. Atmos.* **2018**, *123*, 331. [[CrossRef](#)]
- Orsolini, Y.J.; Manney, G.L.; Santee, M.L.; Randall, C.E. An upper stratospheric layer of enhanced HNO₃ following exceptional solar storms. *Geophys. Res. Lett.* **2005**, *32*. [[CrossRef](#)]
- Nassar, R.; Bernath, P.F.; Boone, C.D.; Clerbaux, C.; Coheur, P.F.; Dufour, G.; Froidevaux, L.; Mahieu, E.; McConnell, J.C.; McLeod, S.D.; et al. A global inventory of stratospheric chlorine in 2004. *J. Geophys. Res.* **2006**, *111*, D22312. [[CrossRef](#)]
- Faxon, C.B.; Allen, D.T. Chlorine chemistry in urban atmospheres: A review. *Environ. Chem.* **2013**, *10*, 221. [[CrossRef](#)]
- Faxon, C.; Bean, J.; Ruiz, L. Inland Concentrations of Cl₂ and ClNO₂ in Southeast Texas Suggest Chlorine Chemistry Significantly Contributes to Atmospheric Reactivity. *Atmosphere* **2015**, *6*, 1487–1506. [[CrossRef](#)]
- Wang, X.; Jacob, D.J.; Eastham, S.D.; Sulprizio, M.P.; Zhu, L.; Chen, Q.; Alexander, B.; Sherwen Ts Evans, M.J.; Lee, B.H.; Haskins, J.D.; et al. The role of chlorine in global tropospheric chemistry. *Atmos. Chem. Phys.* **2019**, *19*, 3981–4003. [[CrossRef](#)]
- Chipperfield, M.P.; Bekki, S.; Dhomse, S.; Harris, N.R.P.; Hassler, B.; Hossaini, R.; Steinbrecht, W.; Thiblemont, R.M.; Weber, M. Detecting recovery of the stratospheric ozone layer. *Nature* **2017**, *549*, 211–218. [[CrossRef](#)]
- Drdla, K.; Müller, R. Temperature thresholds for chlorine activation and ozone loss in the polar stratosphere. *Ann. Geophys.* **2012**, *30*, 1055–1073. [[CrossRef](#)]
- Wegner, T.; Groß, J.-U.; von Hobe, M.; Stroh, F.; Suminska-Ebersoldt, O.; Volk, C.M.; Hösen, E.; Mitev, V.; Shur, G.; Müller, R. Heterogeneous chlorine activation on stratospheric aerosols and clouds in the Arctic polar vortex. *Atmos. Chem. Phys.* **2012**, *12*, 11095–11106. [[CrossRef](#)]
- Nakajima, H.; Wohltmann, I.; Wegner, T.; Takeda, M.; Pitts, M.C.; Poole, L.R.; Lehmann, R.; Santee, M.L.; Rex, M. Polar stratospheric cloud evolution and chlorine activation measured by CALIPSO and MLS, and modeled by ATLAS. *Atmos. Chem. Phys.* **2016**, *16*, 3311–3325. [[CrossRef](#)]
- Neuman, A.; Gao, S.; Fahey, W.; Holecek, C.; Ridley, A.; Walega, G.; Grahek, E.; Richard, C.; Mcelroy, T.; Thompson, L. In situ measurements of HNO₃, NO_y, NO, and O₃ in the lower stratosphere and upper troposphere. *Atmos. Environ.* **2001**, *35*, 5789–5797. [[CrossRef](#)]
- Ungermann, J.; Ern, M.; Kaufmann, M.; Müller, R.; Spang, R.; Ploeger, F.; Vogel, B.; Riese, M. Observations of PAN and its confinement in the Asian summer monsoon anticyclone in high spatial resolution. *Atmos. Chem. Phys.* **2016**, *16*, 8389–8403. [[CrossRef](#)]
- Marcy, T.P.; Gao, R.S.; Northway, M.J.; Popp, P.J.; Stark, H.; Fahey, D.W. Using chemical ionization mass spectrometry for detection of HNO₃, HCl, and ClONO₂ in the atmosphere. *Int. J. Mass Spectrom.* **2005**, *243*, 63–70. [[CrossRef](#)]
- Jurkat, T.; Voigt, C.; Kaufmann, S.; Zahn, A.; Sprenger, M.; Hoor, P.; Bozem, H.; Müller, S.; Dörnbrack, A.; Schlager, H.; et al. A quantitative analysis of stratospheric HCl, HNO₃, and O₃ in the tropopause region near the subtropical jet. *Geophys. Res. Lett.* **2014**, *41*, 3315–3321. [[CrossRef](#)]

17. Johansson, S.; Woiwode, W.; Höpfner, M.; Friedl-Vallon, F.; Kleinert, A.; Kretschmer, E.; Latzko, T.; Orphal, J.; Preusse, P.; Ungermann, J.; et al. Airborne limb-imaging measurements of temperature, HNO₃, O₃, ClONO₂, H₂O and CFC-12 during the Arctic winter 2015/2016: Characterization, in situ validation and comparison to Aura/MLS. *Atmos. Meas. Tech.* **2018**, *11*, 4737–4756. [[CrossRef](#)]
18. Vigouroux, C.; De Maziere, M.; Errera, Q.; Chabrilat, S.; Mahieu, E.; Duchatelet, P.; Wood, S.; Smale, D.; Barthlott, S.; Blumenstock, T.; et al. Comparisons between ground-based FTIR and MIPAS N₂O and HNO₃ profiles before and after assimilation in BASCOE. *Atmos. Chem. Phys.* **2007**, *7*, 377–396. [[CrossRef](#)]
19. Froidevaux, L.; Jiang, Y.; Lambert, A.; Livesey, N.; Read, W.; Waters, J.; Fuller, R.; Marcy, T.; Popp, P.; Gao, R.; et al. Validation of Aura Microwave Limb Sounder HCl measurements. *J. Geophys. Res.* **2008**, *113*, 15–25. [[CrossRef](#)]
20. Wespes, C.; Hurtmans, D.; Clerbaux, C.; Santee, M.L.; Martin, R.V.; Coheur, P.F. Global distributions of nitric acid from IASI/MetOP measurements. *Atmos. Chem. Phys.* **2009**, *9*, 7949–7962. [[CrossRef](#)]
21. Jones, A.; Urban, J.; Murtagh, D.P.; Sanchez, C.; Walker, K.A.; Livesey, N.J.; Froidevaux, L.; Santee, M.L. Analysis of HCl and ClO time series in the upper stratosphere using satellite data sets. *Atmos. Chem. Phys.* **2011**, *11*, 5321–5333. [[CrossRef](#)]
22. Ronsmans, G.; Langerock, B.; Wespes, C.; Hannigan, J.W.; Hase, F.; Kerzenmacher, T.; Mahieu, E.; Schneider, M.; Smale, D.; Hurtmans, D.; et al. First characterization and validation of FORLI-HNO₃ vertical profiles retrieved from IASI/Metop. *Atmos. Meas. Tech.* **2016**, *9*, 4783–4801. [[CrossRef](#)]
23. Ronsmans, G.; Wespes, C.; Hurtmans, D.; Clerbaux, C.; Coheur, P.F. Spatio-temporal variations of nitric acid total columns from 9 years of IASI measurements A driver study. *Atmos. Chem. Phys.* **2018**, *18*, 4403–4442. [[CrossRef](#)]
24. Wunch, D.; Toon, G.C.; Blavier, J.F.; Washenfelder, R.A.; Notholt, J.; Connor, B.J.; Griffith, D.W.; Sherlock, V.; Wennberg, P.O. The total carbon column observing network. *Philos. Trans. A Math Phys. Eng. Sci.* **2011**, *369*, 2087–2112. [[CrossRef](#)]
25. De Mazière, M.; Thompson, A.M.; Kurylo, M.J.; Wild, J.D.; Bernhard, G.; Blumenstock, T.; Braathen, G.O.; Hannigan, J.W.; Lambert, J.-C.; Leblanc, T.; et al. The Network for the Detection of Atmospheric Composition Change (NDACC): History, status and perspectives. *Atmos. Chem. Phys.* **2018**, *18*, 4935–4964. [[CrossRef](#)]
26. Wunch, D.; Wennberg, P.O.; Osterman, G.; Fisher, B.; Eldering, A. Comparisons of the Orbiting Carbon Observatory-2 (OCO-2) XCO₂ measurements with TCCON. *Atmos. Meas. Tech.* **2017**, *10*, 1–45. [[CrossRef](#)]
27. Polyakov, A.V.; Timofeyev, Y.M.; Poberovskii, A.V. Ground-based measurements of total column of hydrogen chloride in the atmosphere near St. Petersburg. *Izv. Atmos. Ocean. Phys.* **2013**, *49*, 411–419. [[CrossRef](#)]
28. Mahieu, E.; Chipperfield, M.P.; Notholt, J.; Reddmann, T.; Anderson, J.; Bernath, P.F.; Blumenstock, T.; Coffey, M.T.; Dhomse, S.S.; Feng, W.; et al. Recent Northern Hemisphere stratospheric HCl increase due to atmospheric circulation changes. *Nature* **2014**, *515*, 104–107. [[CrossRef](#)]
29. Virolainen, Y.; Timofeyev, Y.; Polyakov, A.; Ionov, D.; Kirner, O.; Poberovskiy, A.; Imhasin, H. Comparing Data Obtained from Ground-Based Measurements of the Total Contents of O₃, HNO₃, HCl, and NO₂ and from Their Numerical Simulation. *Izv. Atmos. Ocean. Phys.* **2016**, *52*, 57–65. [[CrossRef](#)]
30. Rinsland, C.P.; Zander, R.; Demoulin, P. Ground-based infrared measurements of HNO₃ total column abundances: Long term trend and variability. *J. Geophys. Res. Atmos.* **1991**, *96*, 9379–9389. [[CrossRef](#)]
31. Nakajima, H.; Murata, I.; Nagahama, Y.; Akiyoshi, H.; Saeki, K.; Kinase, T.; Takeda, M.; Tomikawa, Y.; Dupuy, E.; Jones, N.B. Chlorine partitioning near the polar vortex edge observed with ground-based FTIR and satellites at Syowa Station, Antarctica, in 2007 and 2011. *Atmos. Chem. Phys.* **2020**, *20*, 1043–1074. [[CrossRef](#)]
32. Whaley, C.; Strong, K.; Adams, C.; Bourassa, A.E.; Daffer, W.H.; Degenstein, D.A.; Fast, H.; Fogal, P.F.; Manney, G.L.; Mittermeier, R.L.; et al. Using FTIR measurements of stratospheric composition to identify midlatitude polar vortex intrusions over Toronto. *J. Geophys. Res. Atmos.* **2013**, *118*, 712–783. [[CrossRef](#)]
33. Shan, C.; Wang, W.; Liu, C.; Sun, Y.; Hu, Q.; Xu, X.; Tian, Y.; Zhang, H.; Morino, I.; Griffith, D.W.T.; et al. Regional CO emission estimated from ground-based remote sensing at Hefei site, China. *Atmos. Res.* **2019**, *222*, 25–35. [[CrossRef](#)]
34. Wang, W.; Tian, Y.; Liu, C.; Sun, Y.; Liu, W.; Xie, P.; Liu, J.; Xu, J.; Morino, I.; Velazco, V.A.; et al. Investigating the performance of a greenhouse gas observatory in Hefei, China. *Atmos. Meas. Tech.* **2017**, *10*, 2627–2643. [[CrossRef](#)]
35. Hase, F.; Drouin, B.J.; Roehl, C.M.; Toon, G.C.; Wennberg, P.O.; Wunch, D.; Blumenstock, T.; Desmet, F.; Feist, D.G.; Heikkinen, P.; et al. Calibration of sealed HCl cells used for TCCON instrumental line shape monitoring. *Atmos. Meas. Tech.* **2013**, *6*, 3527–3537. [[CrossRef](#)]
36. Sun, Y.; Liu, C.; Chan, K.; Wang, W.; Shan, C.; Hu, Q.; Liu, J. The Influence of Instrumental Line Shape Degradation on the Partial Columns of O₃, CO, CH₄ and N₂O Derived from High-Resolution FTIR Spectrometry. *Remote Sens.* **2018**, *10*, 2041. [[CrossRef](#)]
37. Rodgers, C.D.; Connor, B.J. Intercomparison of remote sounding instruments. *J. Geophys. Res. Atmosph.* **2003**, *108*. [[CrossRef](#)]
38. Schneider, M.; Sepulveda, E.; Garca, O.; Hase, F.; Blumenstock, T. Remote sensing of water vapour profiles in the framework of the Total Carbon Column Observing Network (TCCON). *Atmos. Meas. Tech.* **2010**, *3*, 1785–1795. [[CrossRef](#)]
39. Kalnay, E.; Kanamitsu, M.; Kistler, R.; Collins, W.; Deaven, D.; Gandin, L.; Iredell, M.; Saha, S.; White, G.; Woollen, J.; et al. The NCEP/NCAR 40-Year Reanalysis Project. *Bullet. Am. Meteorolog. Soc.* **1996**, *77*, 437. [[CrossRef](#)]

40. Rothman, L.S.; Gordon, I.E.; Barbe, A.; Benner, D.C.; Bernath, P.E.; Birk, M.; Boudon, V.; Brown, L.R.; Campargue, A.; Champion, J.P.; et al. The HITRAN 2008 molecular spectroscopic database. *J. Quant. Spectrosc. Radiat. Transf.* **2009**, *110*, 533–572. [[CrossRef](#)]
41. Fu, D.; Walker, K.A.; Mittermeier, R.L.; Strong, K.; Sung, K.; Fast, H.; Bernath, P.F.; Boone, C.D.; Daffer, W.H.; Fogal, P.; et al. Simultaneous trace gas measurements using two Fourier transform spectrometers at Eureka, Canada during spring 2006, and comparisons with the ACE-FTS. *Atmos. Chem. Phys.* **2011**, *11*, 5383–5405. [[CrossRef](#)]
42. Lindenmaier, R.; Strong, K.; Batchelor, R.L.; Chipperfield, M.P.; Daffer, W.H.; Drummond, J.R.; Duck, T.J.; Fast, H.; Feng, W.; Fogal, P.F.; et al. Unusually low ozone, HCl, and HNO₃ column measurements at Eureka, Canada during winter/spring 2011. *Atmos. Chem. Phys.* **2012**, *12*, 3821–3835. [[CrossRef](#)]
43. Thoning, K.W.; Tans, P.P.; Komhyr, W.D. Atmospheric carbon dioxide at Mauna Loa Observatory: 2. Analysis of the NOAA GMCC data. *J. Geophys. Res.* **1989**, *94*, 8549–8565. [[CrossRef](#)]
44. Stolarski, R.S.; Douglass, A.R.; Strahan, S.E. Using satellite measurements of N₂O to remove dynamical variability from HCl measurements. *Atmos. Chem. Phys.* **2018**, *18*, 5691–5697. [[CrossRef](#)]
45. Kohlhepp, R.; Ruhnke, R.; Chipperfield, M.P.; De Mazière, M.; Notholt, J.; Barthlott, S.; Batchelor, R.L.; Blatherwick, R.D.; Blumenstock, T.; Coffey, M.T.; et al. Observed and simulated time evolution of HCl, ClONO₂, and HF total column abundances. *Atmos. Chem. Phys.* **2012**, *12*, 3527–3556. [[CrossRef](#)]
46. Yela, M.; Gil-Ojeda, M.; Navarro-Comas, M.; Gonzalez-Bartolomé, D.; Puentedura, O.; Funke, B.; Iglesias, J.; Rodríguez, S.; García, O.; Ochoa, H.; et al. Hemispheric asymmetry in stratospheric NO₂ trends. *Atmos. Chem. Phys.* **2017**, *17*, 13373–13389. [[CrossRef](#)]
47. Yin, H.; Sun, Y.; Liu, C.; Zhang, L.; Lu, X.; Wang, W.; Shan, C.; Hu, Q.; Tian, Y.; Zhang, C.; et al. FTIR time series of stratospheric NO₂ over Hefei, China, and comparisons with OMI and GEOS-Chem model data. *Opt. Express* **2019**, *27*, A1225–A1240. [[CrossRef](#)]
48. Montzka, S.A.; Dutton, G.S.; Yu, P.; Ray, E.; Portmann, R.W.; Daniel, J.S.; Kuijpers, L.; Hall, B.D.; Mondeel, D.; Siso, C.; et al. An unexpected and persistent increase in global emissions of ozone-depleting CFC-11. *Nature* **2018**, *557*, 413–417. [[CrossRef](#)]
49. Polyakov, A.V.; Timofeyev, Y.M.; Virolainen, Y.A.; Makarova, M.V.; Poberovskii, A.V.; Imhasin, H.K. Ground-Based Measurements of the Total Column of Freons in the Atmosphere near St. Petersburg (2009–2017). *Izv. Atmosf. Ocean. Phys.* **2018**, *54*, 487–494. [[CrossRef](#)]
50. Khosrawi, F.; Urban, J.; Lossow, S.; Stiller, G.; Weigel, K.; Braesicke, P.; Pitts, M.C.; Rozanov, A.; Burrows, J.P.; Murtagh, D. Sensitivity of polar stratospheric cloud formation to changes in water vapour and temperature. *Atmos. Chem. Phys.* **2016**, *16*, 101–121. [[CrossRef](#)]
51. Yin, H.; Sun, Y.; Liu, C.; Lu, X.; Smale, D.; Blumenstock, T.; Nagahama, T.; Wang, W.; Tian, Y.; Hu, Q.; et al. Ground-based FTIR observation of hydrogen chloride (HCl) over Hefei, China, and comparisons with GEOS-Chem model data and other ground-based FTIR stations data. *Opt. Express* **2020**, *28*, 8041–8055. [[CrossRef](#)] [[PubMed](#)]
52. Webster, C.R.; May, R.D.; Jaegle, L.; Hu, H.; Sander, S.P.; Gunson, M.R.; Toon, G.C.; Russell, J.M.; Stimpfle, R.M.; Koplrow, J.P.; et al. Hydrochloric-Acid and the Chlorine Budget of the Lower Stratosphere. *Geophys. Res. Lett.* **1994**, *21*, 2575–2578. [[CrossRef](#)]
53. Solomon, S. Stratospheric Ozone Depletion: A Review of Concepts and History. *Rev. Geophys.* **1999**, *37*, 275–316. [[CrossRef](#)]
54. Waters, J.W.; Froidevaux, L.; Harwood, R.S.; Jarnot, R.F.; Pickett, H.M.; Read, W.G.; Siegel, P.H.; Cofield, R.E.; Filipiak, M.J.; Flower, D.A.; et al. The Earth Observing System Microwave Limb Sounder (EOS MLS) on the Aura satellite. *IEEE Trans. Geosci. Remote Sens.* **2006**, *44*, 1075–1092. [[CrossRef](#)]
55. Froidevaux, L.; Livesey, N.J.; Read, W.G.; Salawitch, R.J.; Waters, J.W.; Drouin, B.; MacKenzie, I.A.; Pumphrey, H.C.; Bernath, P.; Boone, C.; et al. Temporal decrease in upper atmospheric chlorine. *Geophys. Res. Lett.* **2006**, *33*, L23813. [[CrossRef](#)]
56. Santee, M.L.; Manney, G.L.; Livesey, N.J.; Froidevaux, L.; Schwartz, M.J.; Read, W.G. Trace gas evolution in the lowermost stratosphere from Aura Microwave Limb Sounder measurements. *J. Geophys. Res.* **2011**, *116*, D18306. [[CrossRef](#)]
57. Livesey, N.J.; Read, W.G.; Wagner, P.A.; Froidevaux, L.; Lambert, A.; Manney, G.L.; Millán, L.F.; Pumphrey, H.C.; Santee, M.L.; Schwartz, M.J.; et al. Version 4.2x Level 2 Data Quality and Description Document. Earth Observing System (EOS) Aura Microwave Limb Sounder (MLS). Available online: https://mls.jpl.nasa.gov/data/v42_data_quality_document.pdf (accessed on 9 February 2017).
58. Buschmann, M.; Deutscher, N.M.; Sherlock, V.; Palm, M.; Warneke, T.; Notholt, J. Retrieval of xCO₂ from ground-based mid-infrared (NDACC) solar absorption spectra and comparison to TCCON. *Atmosf. Measur. Tech.* **2016**, *9*, 577–585. [[CrossRef](#)]